Uncertainty Determination for Aeroheating in Uranus and Saturn Probe Entries by the Monte Carlo Method

Grant Palmer, Dinesh Prabhu, Brett A. Cruden
ERC, Inc. at NASA Ames Research Center, Moffett Field, CA 94035

Abstract

The 2013-2022 Decaedal survey for planetary exploration has identified probe missions to Uranus and Saturn as high priorities. This work endeavors to examine the uncertainty for determining aeroheating in such entry environments. Representative entry trajectories are constructed using the TRAJ software. Flowfields at selected points on the trajectories are then computed using the Data Parallel Line Relaxation (DPLR) Computational Fluid Dynamics Code. A Monte Carlo study is performed on the DPLR input parameters to determine the uncertainty in the predicted aeroheating, and correlation coefficients are examined to identify which input parameters show the most influence on the uncertainty. A review of the present best practices for input parameters (e.g. transport coefficient and vibrational relaxation time) is also conducted. It is found that the 2σ-uncertainty for heating on Uranus entry is no more than 2.1%, assuming an equilibrium catalytic wall, with the uncertainty being determined primarily by diffusion and H_2 recombination rate within the boundary layer. However, if the wall is assumed to be partially or non-catalytic, this uncertainty may increase to as large as 18%. The catalytic wall model can contribute over 3x change in heat flux and a 20% variation in film coefficient. Therefore, coupled material response/fluid dynamic models are recommended for this problem. It was also found that much of this variability is artificially suppressed when a constant Schmidt number approach is implemented. Because the boundary layer is reacting, it is necessary to employ self-consistent effective binary diffusion to obtain a correct thermal transport solution. For Saturn entries, the 2σ uncertainty for convective heating was less than 3.7%. The major uncertainty driver was dependent on shock temperature/velocity, changing from boundary layer thermal conductivity to diffusivity and then to shock layer ionization rate as velocity increases. While radiative heating for Uranus entry was negligible, the nominal solution for Saturn computed up to 20% radiative heating at the highest velocity examined. The radiative heating followed a non-normal distribution, with up to a 3x variation in magnitude. This uncertainty is driven by the H_2 dissociation rate, as H_2 that persists in the hot non-equilibrium zone contributes significantly to radiation.

I. Background

To build a sustainable program in thermal protections system (TPS) development for Outer Planet exploration, it is important to develop and maintain state-of-the-art models for shock layer thermochemistry and gas phase transport of mass, momentum and energy. Chemical kinetics and transport models are at the heart of building design databases of entry aerothermal environments, and knowledge of uncertainties in these models is essential in developing a design margins policy. As experimental and simulation techniques improve, these uncertainties can be reduced thus leading to more mass efficient designs of the entry system.

The atmospheres of the Outer Planets – Jupiter, Saturn, Uranus and Neptune – are composed mainly of H_2 and He. Other trace species and particularly CH_4 are present in the troposphere, but for entry purposes (except Neptune) are irrelevant. The high-temperature reaction mechanisms and chemical kinetics currently employed in flowfield simulation tools are based on models from the 1970s.[1] These heritage models were constructed based primarily on experimental data available at that time. Recent advances in computing capability have allowed the use of *ab initio* methods in quantum chemistry to predict properties for many electron systems more accurately. Additionally, improvements in experimental techniques also allow better ways to assess heritage data. However, uncertainties are as yet unknown for some fundamental properties and mechanisms because they have not been rigorously assessed. In recent years, methods have been developed for assessing uncertainties for a variety of entry conditions, include Lunar return,[2,3] Titan probes[4, 5] and Mars Aerocapture[6]. These methods have allowed margins based on real uncertainties to be assigned to aerothermal predictions and for the identification of sources of uncertainties and their quantification.

The first phase of this task was to focus on the assessment of aeroheating uncertainty using the current state-of-the-art models. This was to be done by applying the current simulation best practices to proposed mission studies. Baseline aeroheating predictions are typically made using computational fluid dynamics (CFD) simulation tools to represent the complex phenomena that occur in the shock layer. It is well known that aeroheating predictions from CFD computations are sensitive to physical, chemical, and numerical models employed, as well as the multitude of parameters introduced in these models[7]. The uncertainty in these predictions, which is a critical element of the overall entry system risk, is the result of a combined effect of stochastic, parametric and structural uncertainties in the models. Stochastic uncertainties are due to random fluctuations in the applied environment, including atmospheric and trajectory dispersions. Parametric uncertainties are due to imprecise measurements or estimates of input parameters, such as reaction rates, thermal relaxation times, transport properties, etc. Structural uncertainties are caused by deficiencies in the formulation of the physical and/or numerical models chosen to represent the true environment. Although prior aerothermal investigations recognize these uncertainties, their effects on the final aeroheating uncertainty have not been rigorously assessed for outer planet entries. Traditional approaches for dealing with these uncertainties have been somewhat *ad hoc*, often relying on expert judgment to assign uncertainty levels to the various elements of the aeroheating predictions and TPS sizing estimates[7]. Large uncertainties in estimating the aerothermal environment could result in an overly conservative safety margin for the TPS, which would cause a significant mass penalty to the vehicle and possibly a reduced mission design space. For the purposes of design and system risk assessment, the uncertainty limits associated with an aeroheating prediction are almost as important as the aeroheating value itself, especially when the limits are large.

This paper includes three additional sections. Section II describes the relevant studies selected based on the Decadal Survey [8] and internal studies, identifying proposed probe missions to Uranus and Saturn. Section III describes the evaluation and improvements to transport coefficients used in the CFD solver, *DPLR* [9]– the preferred aerothermal simulation tool at NASA Ames Research Center. Section IV, being the major part of this study, describes a systematic Monte Carlo uncertainty and sensitivity analysis performed on the key parametric uncertainties, including both convective and radiative heating components.

II. Outer Planet Trajectories

The missions of relevance to the present study were derived from the National Research Council's Decadal Survey, performed from 2009-2011.[8] The Decadal Survey outlines the highest priority science goals for planetary exploration for the ten years from 2013-2022. Of the fifteen potential missions included in the Decadal Survey, two involved planetary probes to the Outer Planets, notably to Saturn and Uranus. A Saturn Probe is recommended as one of seven candidates for a New Frontiers-class mission. The primary objectives of this probe are to determine the noble gas abundances, isotopic ratios of selected elements, and to study the structure of the atmosphere of Saturn. An orbiter and entry probe to Uranus were recommended as one of three priorities for Flagship-class missions. Although the Uranus mission was considered the lowest priority of the three, the recommended scenarios all included its initiation even as one the higher priority missions (Jupiter Europa Orbiter) could be eliminated under budget constraints. The major objectives of the Uranus mission are to examine the ring system and the interior structure, composition and atmosphere of Uranus.

Appendices to the Decadal Survey included detailed mission architecture studies for every mission considered. Appendices 19 and 20 detailed the probe trade and mission studies,[10, 11] respectively, for Saturn entry. Appendix 24 detailed the concept approach for Uranus or Neptune entry, prioritizing (and further developing) that of Uranus.[12]

The entry state from the Saturn mission study was used to develop an entry trajectory in the present work. This entry state involved a 216 kg entry probe (1 m dia. aeroshell) entering at a latitude of -22.4º, and a flight path angle of -8º. The atmosphere-relative entry velocity was 26.9 km/s. A second trajectory examined in this work was selected from an internal (Ames/Langley) study commissioned by NASA's In-Space Propulsion Technology (ISPT) program in 2012. This study examined the trade space – entry velocity, ballistic coefficient, and entry flight path angle – to determine viable entries (both high latitude and equatorial). The representative trajectory included here from that study had a much steeper descent at -15º and atmosphere relative velocity of 28.2 km/s.

For the case of Uranus, the present work relied upon Appendix 24 of the Decadal Survey. For an entry velocity of 22.3 km/s and an entry flight path angle of -68°, a flight trajectory was developed for a 127 kg entry mass probe of 0.76 m diameter. The probe was a 45° sphere-cone geometry, similar to ones used in the Pioneer Venus and Galileo missions.

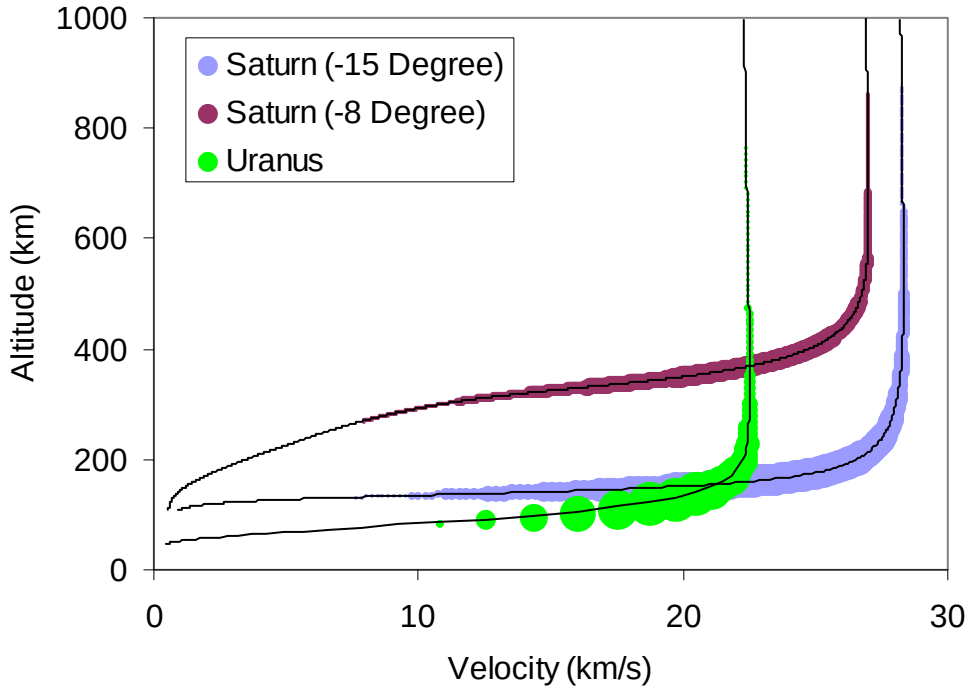

Figure 1. Trajectories examined in this work. The size of each point shown is proportional to the predicted heat flux.

3DOF entry trajectories were generated with *TRAJ*.[13] *TRAJ* is a program capable of generating trajectories for any planetary entry scenario given an entry condition. *TRAJ* also uses established correlations to estimate radiative and convective heating at the stagnation point of the entry probe along its flight trajectory. The three entry trajectories developed using *TRAJ* are shown in the altitude-velocity map in Figure 1. The width of the points on the line represents the heating magnitude. For the Uranus trajectory a peak total heat flux of 5.1 kW/cm^2 and a total heat load of 32.8 kJ/cm^2 are estimated from *TRAJ*. These numbers are 9-14% lower than the decadal study estimate of 5.5 kW/cm^2 and 38.1 kJ/cm^2. For the steeper Saturn trajectory a peak total heat flux of 3.0 kW/cm^2 and a total heat load of 130 kJ/cm^2 are estimated, while for the shallower entry the estimated peak flux was 1.3 kW/cm^2 and the total heat load was 257 kJ/cm^2. This large total heat load is the result of a much slower rate of descent, resulting in a 4-5× increase in the width of the heat pulse. The decadal report gave no estimated heat flux for comparison to these numbers. *TRAJ*'s correlations for radiative heating found the radiative heating to be insignificant in comparison to convection for all three of these trajectories. However, more detailed simulations under current best practices suggest this result to be incorrect, as will be shown in Section IV. It is expected that this study will help to better improve these correlations in the future.

III. Evaluation of CFD Parameters

The databases employed by *DPLR* for H_2/He are assumed to represent the current state-of-the-art in modeling for Outer Planets entry. In this section, we review some of the parameters employed and

assess their accuracy. These parameters are revised based on critical evaluation of existing literature, as described below. The updated parameters are used for the further study in Section IV.

Collision Integrals

Collision integrals are used for computation of transport properties – viscosity, diffusivity and thermal conductivity – of the flow medium (mixture of gases). Each of these flow properties is generally calculated for every possible interaction of two species (i.e. binary model), then the property of the gas mixture is calculated from these pairwise interactions via mixing rules. Therefore, it is necessary to have $n(n+1)/2$ interaction parameters, where n is the number of species. *DPLR* uses a first-order approach to determining transport properties, and therefore there are two collision integrals required for each interaction. Higher-order solutions, which would require the knowledge of additional collision integrals, have been investigated by Palmer and Wright for air chemistry and found to have negligible impact.[14]

Generally, the collision integrals are obtained through evaluation of differential scattering cross-sections between species. While these are in some cases investigated experimentally, they are often more readily calculated through quantum mechanics. The collision integrals used in *DPLR* were obtained through extensive evaluation in the literature, the collection of which has been summarized in two publications for Mars[15] and Air[16] mixtures. A third paper for hydrogen/helium mixtures was never published.[17] A recent publication by Bruno *et al.*,[18] performed an in-depth evaluation of literature data and their own empirical models to obtain the collision integrals up to 5th order. As an assessment of the uncertainty, the results of Bruno *et al.* are compared against those already employed in *DPLR*.

Interactions between two charged particles can be accurately calculated by Coulombic theory and therefore do not require review here. For interactions involving at least one neutral species, *DPLR* uses the Gupta parameterization[19] of the collision integral:

$$\Omega = DT^{A(\ln T)^2 + B\ln T + C} \tag{4}$$

The Bruno collision integrals have been re-fit to this form and incorporated into *DPLR* when believed to be more accurate. Below is a summary of this evaluation:

Neutral-Neutral Interactions

The neutral interactions include H-H, H-H_2, H_2-H_2, He-He, H-He and H_2-He. For the first four pairs of these interactions, *DPLR* and Bruno use the same data sources — the *ab initio* studies of Stallcop *et al.*[20, 21] The study of Stallcop *et al.* is highly accurate, citing an error of 1%. While this level of accuracy is difficult to confirm experimentally, the collision integrals do predict the viscosity of gaseous hydrogen (the measurement of which is also highly accurate) to within this level. The H-H collision integrals show near perfect agreement with the older estimates of Yos,[22] suggesting these values to be well established. The *DPLR* and Bruno values agree to within the accuracy of their parameterization, which is within a few percent above 300K. At lower temperatures, a somewhat larger deviation (up to ~30%) may exist due to the limitations of the Gupta formula.

For H-He and H_2-He, *DPLR* utilizes unpublished data from Stallcop generated using the same methodology as with the other neutral interactions. As a result, the DPLR data set is about 10% and 40% lower, respectively, for each of these. These *DPLR* values are believed to be more accurate.

H^+ *interactions*

The proton interactions in *DPLR* and Bruno are both based on the *ab initio* work of Krstic.[23, 24] The data of Krstic are expected to be of high accuracy. The data, however, must be extrapolated below 0.1 eV. As a result, the interactions from *DPLR* and Bruno differ by as much as 12% above 1000K, and even further at lower temperature. The extrapolation approach of Bruno *et al.* is physically based, as opposed to the purely numerical approach used in the *DPLR* database. Therefore, the collision integrals of Bruno *et al.* are recommended.

e^- *interactions*

There are three electron interactions, only two of which are actually parameterized by *DPLR*. Above 1000K, the collision integrals for e^--H and e^--H_2 agree within 50% between the two databases. At low temperature, the *DPLR* parameterization diverges. The electron collision integrals from Bruno *et al.* are based on newer electron scattering databases than used in *DPLR*. For e^--H_2, we have re-evaluated the collision integrals using alternative data sources and found the results to be in good agreement with that of Bruno. Until a more detailed evaluation can be undertaken, it is recommended that all three e^- interactions of Bruno *et al.* be adopted.

H_2^+ *and* He^+ *interactions*

H_2^+ and He^+ are minor species under all relevant conditions, and as such their collision integrals have no real impact on simulation results. Nevertheless, their values have been assessed. The deviation between the two data sets is substantial, between 35-100%. For He^+-H and He^+-He, Bruno *et al.* use newer *ab initio* potentials to calculate the collision integrals, while *DPLR* used a combination of older experimental and empirical studies. Bruno *et al.* use a phenomenological model to describe the He^+-H_2, H_2^+-H, H_2^+-He and H_2^+-H_2 interactions.[25] The *DPLR* values for these generally come from older sources that are not as well validated. The H_2^+-H evaluation is based on the *ab initio* method from Krstic,[23] so is the only one of these interactions that is assumed to be more accurate in *DPLR*. For all other interactions, the values of Bruno *et al*. are recommended.

The summary of these parameterizations, and their sources, are given below in Table 1. The most recent release of *DPLR* (v. 4.03.1) has been updated to use these values.

Table 1. Gupta parameters for collision integrals in this work.

Species	Collision Integral	Gupta Parameter				Data Source	Reference
		A	B	C	D		
H-H	$\Omega^{(1,1)}$	-1.88E-02	3.59E-01	-2.51E+00	1.15E+04	DPLR	[20]
	$\Omega^{(2,2)}$	-1.99E-02	4.13E-01	-3.10E+00	7.59E+04		
H-H_2	$\Omega^{(1,1)}$	-1.47E-03	-2.79E-02	2.27E-01	1.50E+01		[21]
	$\Omega^{(2,2)}$	-3.31E-03	8.68E-03	2.65E-02	2.40E+01		
H-He	$\Omega^{(1,1)}$	-6.82E-03	1.06E-01	-8.08E-01	1.66E+02		[17]
	$\Omega^{(2,2)}$	-7.67E-03	1.28E-01	-9.53E-01	2.66E+02		
H_2-H_2	$\Omega^{(1,1)}$	-5.62E-03	9.77E-02	-7.95E-01	2.18E+02		[20]
	$\Omega^{(2,2)}$	-5.46E-03	9.60E-02	-7.67E-01	2.21E+02		
H_2-He	$\Omega^{(1,1)}$	-3.49E-03	5.10E-02	-4.60E-01	8.39E+01		[17]
	$\Omega^{(2,2)}$	-3.46E-03	5.24E-02	-4.62E-01	9.41E+01		
He-He	$\Omega^{(1,1)}$	-3.58E-03	5.68E-02	-5.14E-01	7.29E+01		
	$\Omega^{(2,2)}$	-5.25E-03	9.66E-02	-8.03E-01	1.65E+02		
H-H^+	$\Omega^{(1,1)}$	-9.97E-04	2.26E-02	-3.19E-01	5.04E+02	Bruno *et al.* [18]	[24]
	$\Omega^{(2,2)}$	-2.39E-02	4.70E-01	-3.31E+00	2.02E+05		
H_2-H^+	$\Omega^{(1,1)}$	-1.80E-02	3.22E-01	-2.17E+00	1.07E+04		[23]
	$\Omega^{(2,2)}$	-8.37E-03	1.49E-01	-1.17E+00	1.43E+03		
He-H^+	$\Omega^{(1,1)}$	-2.05E-02	3.91E-01	-2.91E+00	7.60E+04		[24]
	$\Omega^{(2,2)}$	-2.73E-02	5.60E-01	-4.18E+00	1.26E+06		
H-e^-	$\Omega^{(1,1)}$	-6.18E-03	6.82E-02	-2.01E-01	4.47E+01		[26, 27]
	$\Omega^{(2,2)}$	-1.90E-03	-3.28E-02	5.05E-01	9.10E+00		
H_2-e^-	$\Omega^{(1,1)}$	-2.27E-02	4.64E-01	-2.90E+00	2.71E+03		[28, 29]
	$\Omega^{(2,2)}$	-1.95E-02	3.89E-01	-2.30E+00	3.72E+02		
He-e^-	$\Omega^{(1,1)}$	-8.24E-03	1.68E-01	-1.06E+00	4.65E+01		[30]
	$\Omega^{(2,2)}$	-6.49E-03	1.20E-01	-6.91E-01	1.95E+01		
H-He^+	$\Omega^{(1,1)}$	-1.78E-02	2.82E-01	-1.64E+00	9.30E+02		[31]
	$\Omega^{(2,2)}$	-1.62E-02	2.83E-01	-1.86E+00	1.95E+03		
H_2-He^+	$\Omega^{(1,1)}$	2.91E-04	1.54E-02	-7.92E-01	2.86E+03		[18]
	$\Omega^{(2,2)}$	-1.15E-03	3.91E-02	-8.74E-01	2.81E+03		
He-He^+	$\Omega^{(1,1)}$	8.24E-04	-2.19E-02	3.89E-02	1.15E+02		[32, 33]
	$\Omega^{(2,2)}$	-8.77E-03	1.50E-01	-1.09E+00	7.53E+02		
H-H_2^+	$\Omega^{(1,1)}$	1.31E-02	-2.21E-01	6.32E-01	1.65E+02	DPLR	[23]
	$\Omega^{(2,2)}$	1.60E-02	-2.89E-01	1.17E+00	4.37E+01		
H_2-H_2^+	$\Omega^{(1,1)}$	-4.44E-03	1.24E-01	-1.33E+00	6.76E+03	Bruno *et al.* [18]	[18, 34]
	$\Omega^{(2,2)}$	1.66E-02	-3.04E-01	1.29E+00	3.65E+01		
He-H_2^+	$\Omega^{(1,1)}$	-7.73E-03	2.30E-01	-2.40E+00	5.49E+04		[18]
	$\Omega^{(2,2)}$	-5.51E-03	1.82E-01	-2.06E+00	2.63E+04		

Vibrational relaxation time

The vibrational relaxation time is an important parameter in predicting non-equilibrium time scales. The vibrational relaxation in *DPLR* is calculated using the Millikan-White formalism[35]:

$$p\tau_v = \exp\left[a\left(T^{-1/3} - b\right) - 18.42 \right] atm - s \qquad (5)$$

As with the collision integrals, this parameter is calculated for binary interactions and then averaged using mixing rules. The values for *a* and *b* are often determined through analysis of shock tube data. Alternatively, there is a generalized Millikan formula that derives *a* and *b* based on the molecular weight and vibrational constant of the species of interest. The existing *DPLR* database had identified values for H_2 relaxation in the literature, but did not use these by default. Instead, they were calculated by the general Millikan formula which gave numbers that were orders of magnitude too large. More recently, Kim *et al.*, have calculated the H_2 relaxation values using a state-to-state model.[36] These results were later presented as a parameterized power law relationship rather than the Millikan-White formula and required different parameterizations at low and high temperature.[37] We have used the Millikan-White formula to refit this parameterization over the entire temperature range, augmenting the fit with the data of Dove and Teitelbaum at low temperature.[38] These fits are given in Figure 2 below, and corresponding parameters in Table 2. It is apparent that the Millikan-White formula gives a good fit over most of the temperature range, except for the region near 5000K where the Park parameterization displays significant slope discontinuity. Since the raw data used to produce this parameterization were not presented by Kim *et al.*, it is assumed reasonable to replace this discontinuity with a smooth function.

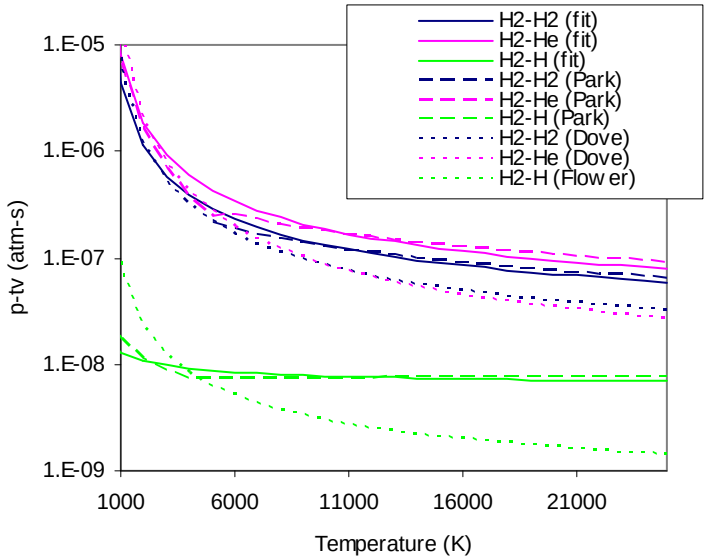

Figure 2. Parameterization of vibrational relaxation time, p-τ_v.

Table 2. Millikan-White Parameters for H_2

Interaction	Parameters	
	A	*b*
H_2-H_2	65.110	0.006821
H_2-He	69.971	0.004682
H_2-H	9.673	0.07250

The affect of updating these parameters is shown in Figure 3. Simulations are shown for the Saturn t=206s and Uranus t=34.5s trajectory points discussed in Section IV. The parameters given in Table 1 and Table 2 are included in the *DPLR* version 4.03.1, which is compared against the previous version, 4.02.2. Figure 3(a) shows the temperature profiles along the stagnation line while Figure 3(b) shows the mole fractions of H_2, H and e^-. For Uranus, the 4.02.2 and 4.03.1 lines lie right on top of each other, indicating that alteration of these parameters have no impact on the shock structure. For Saturn, however, a significant change in the T-T_v coupling is observed. This is due to the multiple order of magnitude increase in T-T_v energy exchange rate, which results in the values of T

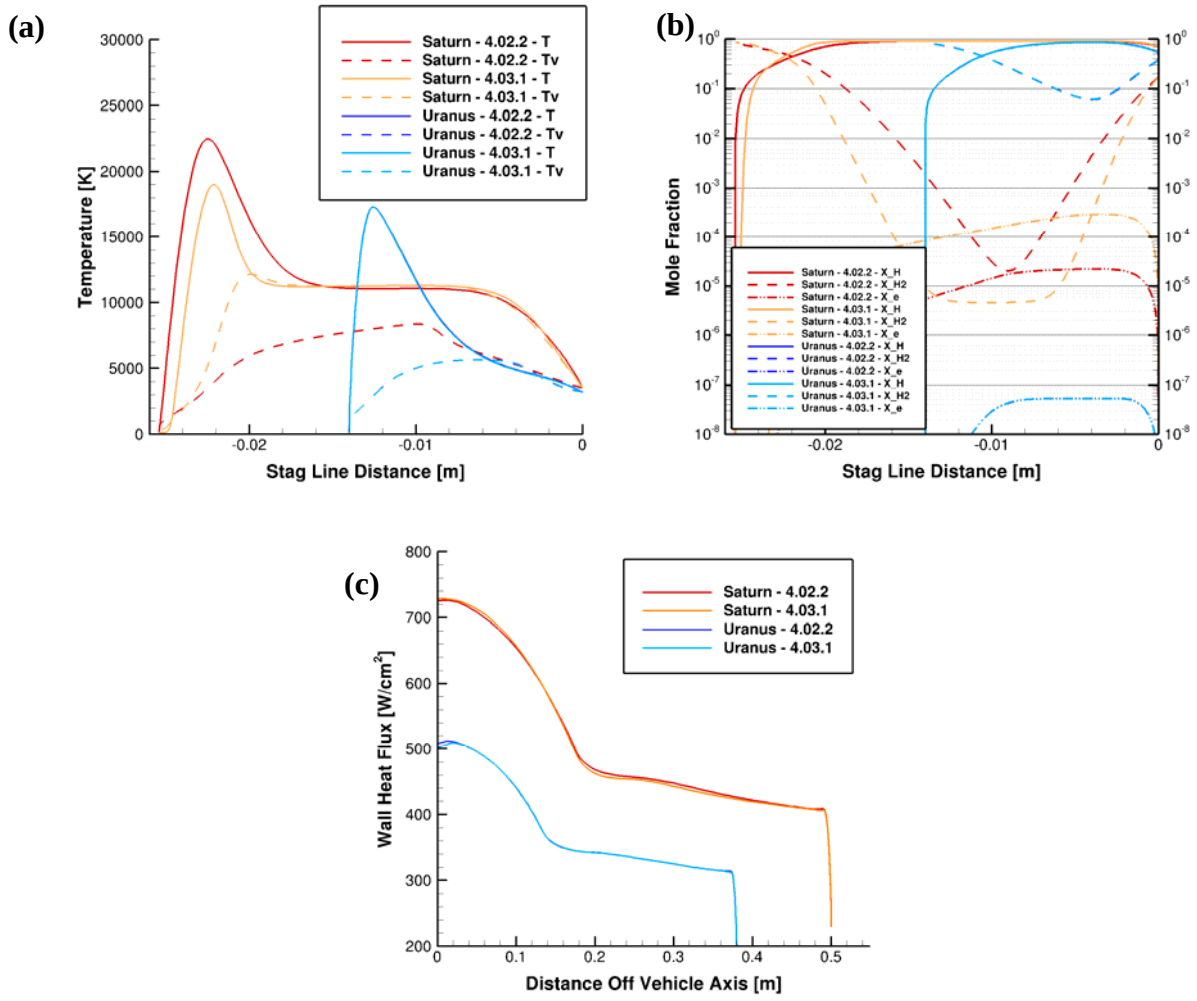

Figure 1. Comparison of DPLR results using the old and new database values: (a) Temperature profiles, (b) Selected mole fractions, and (c) Convective heating along the outer mold line.

and T_v approaching one another much faster behind the shock front. This has the effect of decreasing T and increasing T_v, while reducing the magnitude and duration of non-equilibrium overshoot. With a faster temperature equilibration comes a more rapid chemical equilibration, as observed in Figure 3(b). Figure 3(c), however, shows that the convective heating is only slightly altered by the change in shock characteristics. Radiative heating, on the other hand, is expected to increase significantly due to its strong dependence on T_v. The cases discussed in Section IV reflect this.

IV. Monte Carlo uncertainty study

General Methodology

The *DPLR* CFD flow code solves the reacting Navier-Stokes equations assuming the gas is in thermochemical non-equilibrium. In addition to mass (for each species) and momentum conservation equations, two energy equations are solved; a total energy equation and a vibro-electronic energy equation. In this formulation it is assumed that the vibrational and electronic modes of the gas are in equilibrium with each other, but not with the translational-rotational component. The 7-species [H_2, H_2^+, H, H^+, He, He^+, e^-] chemistry of Leibowitz[1] was used. Viscosity and thermal conductivity are modeled using the species expressions and mixing rules presented by Gupta *et al.* [19] The Self-Consistent Effective Binary Diffusion (SCEBD) model was used to compute diffusion. Many of the cases assumed an equilibrium catalytic surface model, but other catalytic surfaces were also investigated. A radiative equilibrium boundary condition is applied, with a constant emissivity of 0.85. The flow was assumed laminar in all cases.

The physical models used by a real-gas CFD flow solver such as the *DPLR* [9] code make use of up to hundreds of input parameter values, depending on the number of species involved. These input parameters are used to define such things as reaction rates or transport property coefficients. CFD codes generally use a single, nominal value for each one of these input parameters, but in reality there is a range of uncertainty associated with each value. A Monte Carlo parametric sensitivity and uncertainty analysis involves generating a statistically meaningful number of solutions where the values of selected input parameters are randomly varied from their nominal values according to a selected distribution function. In this study, a Gaussian distribution function was assumed to determine the input parameter variation. The statistical data can be analyzed to determine the fractional contribution of each input parameter to the overall variability of a selected output variable (stagnation point heating for example). The 2σ and/or 3σ range can be calculated for an output variable to assign confidence levels to the nominal CFD solution values.

As was noted by Wright *et al.* [39], for a non-linear system with many inputs contributing to output values, it is not possible to rigorously separate the contribution of any one input to any one output. However, a linear regression analysis can be used to approximately determine the uncertainty contributions. Under linear regression, the square of the correlation coefficient, r_{ij}, is given by the following equation:

$$r_{ij}^2 = \frac{\left(\sum_{k=1}^{n} (x_{ki} - \bar{x}_i)(y_{kj} - \bar{y}_j) \right)^2}{n^2 \sigma^2(x_i) \sigma^2(y_j)} \quad (1)$$

The correlation coefficient can be interpreted as the fractional contribution to the uncertainty of output variable, y_j, due to uncertainty in input parameter, x_i. In Eq. (1), the x variables refer to input parameters, and the y variables indicate output parameters. Nominal values of input or output variables are $\bar{x}_i$ and $\bar{y}_j$. The total number of Monte Carlo simulations is equal to n. The σ^2 terms in the denominator of Eq. (1) are the variances of the input and output parameters.

$$\sigma^2(x_i) = \frac{1}{n} \sum_{k=1}^{n} x_{ki}^2 - \left(\frac{1}{n} \sum_{k=1}^{n} x_{ki} \right)^2 \quad (2)$$

A statistically meaningful number of solutions is one that is sufficiently high such the statistical results approach an asymptotic value. It was found by tracking statistical results that 2000 solutions were sufficient to provide converged statistical results for Uranus and Saturn entries. CFD input parameters that were perturbed in the Monte Carlo process include reaction rates, vibrational-translational relaxation times, and binary collision integrals used in the computation of diffusion, viscosity, and thermal conductivity. Since this work focuses on laminar, non-blowing flow environments, input parameters relating to bulk material properties, material response, and turbulence models are not considered.

Table 3. Input parameters and sensitivity ranges for outer planet entry analysis.

Input category	Model	Parameter varied	Variability for sensitivity analysis
Dissociation reaction rates	$k=A_M T^{\eta} \exp(-D/T_a)$	A_M	± 1 order of magnitude
Exchange reaction rates	$k=A\ T^{\eta} \exp(-D/T_a)$	A	± 1 order of magnitude
V-T Relaxation time	Millikan and White/Camac[6]	a and b parameters	1.05-4x
Binary collision integral	$\Omega^{(1,1)}$, $\Omega^{(2,2)}=A\ f(T)$	A	±10% for neutral-neutral, ±50% for all others

Because of the large number of input parameters involved, it would be problematic to come up with precise uncertainty estimates for each of them. Instead, the first step in the sensitivity/uncertainty process is to perform the statistical analysis where the values of all of the input parameters are varied within conservative uncertainty ranges that are held constant for each input parameter type. Table 4 shows the five general categories of input parameters included in the Monte Carlo analysis and the range of variability used in the sensitivity analysis. The reaction rate uncertainties are based upon our commonly expected uncertainty for kinetic models. The V-T relaxation rates were chosen to encompass the range of data shown in Figure 2 and are different for each parameter. The

uncertainties in binary collision integrals are based upon the analysis of Section III and may be conservative for many of the neutral-neutral interactions.

Statistically, uncertainty is defined as the standard error from the mean of a sample of measurements. However, since multiple measurements are rare for the input parameters that are being considered in this work, the uncertainties in the parameters will be mostly estimated or, in some cases, taken from the literature. Estimation of uncertainties associated with the input parameters is often a subjective issue on which experts may express differing opinions. The ranges used in this study were similar to those Refs. [2-6], but some changes were made to the H and He collision integral ranges for the Uranus and Saturn gas mixtures. A preprocessing code is used to perturb the nominal input parameter values according to a Gaussian distribution and generate the *DPLR* input files. Once the *DPLR* computations are complete, correlation coefficients are computed for each input-output pair using a linear regression analysis and the fractional contribution of each input parameter variation to the output parameter variation is obtained.

Depending on vehicle geometry and entry conditions, radiative heating rates at the vehicle surface may be significant (or even dominant). The same Monte Carlo approach that was applied to study convective heating rate variability can be applied to radiative heating rate variability. In this case, the temperatures and species number densities from the *DPLR* CFD Monte Carlo solutions are provided as inputs to the *NEQAIR* line-by-line radiation code [40] to determine which CFD code input parameters have the greatest effect on radiative heating rate. The *NEQAIR* code computes the emission and absorption spectra along a line-of-sight (LOS) for atomic species, molecular species electronic band systems, and infrared band systems. The radiative heating rate is determined using either a tangent slab or spherical cap assumption. Individual electronic transitions are evaluated for atomic and molecular species. The code can model the bound-free and free-free continuum radiation caused by interactions of electrons with neutral and ionized atomic species. *NEQAIR* is currently used to compute radiative heating as part of the Crew Exploration Vehicle (CEV) Computational Aerosciences Project (CAP) and has been validated against shock tube experimental data in both air [41] and CO_2 gas mixtures [42].

Table 4. Freestream and wall conditions, Uranus Monte Carlo simulations.

t (sec)	ρ_∞ (kg/m^3)	T_∞ (K)	V_∞ (km/s)	q_w(conv) (W/cm^2)	q_w(rad) (W/cm^2)	T_w (K)
34.5	2.04e-5	128.2	22.503	542	4.6	3258
36.5	4.86e-5	118.5	22.459	725	4.5	3502
42.5	2.47e-3	66.36	19.716	1942	0.02	4480

Results - Uranus Entries

Monte Carlo simulations were performed for the trajectory discussed in Section II. The freestream mass fractions of H_2 and He were assumed to be 0.7405 and 0.2595 respectively (0.85 and 0.15 by mole fraction). Calculations were performed at three points along the trajectory shown in Table 4.

This first set of Monte Carlo simulations was generated using an equilibrium catalytic wall boundary condition. Also shown in Table 4 are stagnation point convective heating rate, radiative heating rate, and radiative equilibrium wall temperature for the nominal solutions. The heating rates determined by CFD were between 30-60% less than those estimated by *TRAJ*. The t=42.5 s condition is the peak convective heating point, per *TRAJ*. The other two cases will experience greater non-equilibrium effects in the shock layer compared to the peak heating point. The stagnation point convective heating rate is significant in all cases. Conversely, the radiative heating rates are negligible in all three cases, so the Monte Carlo analysis was only applied to the convective heating rate for the Uranus simulations.

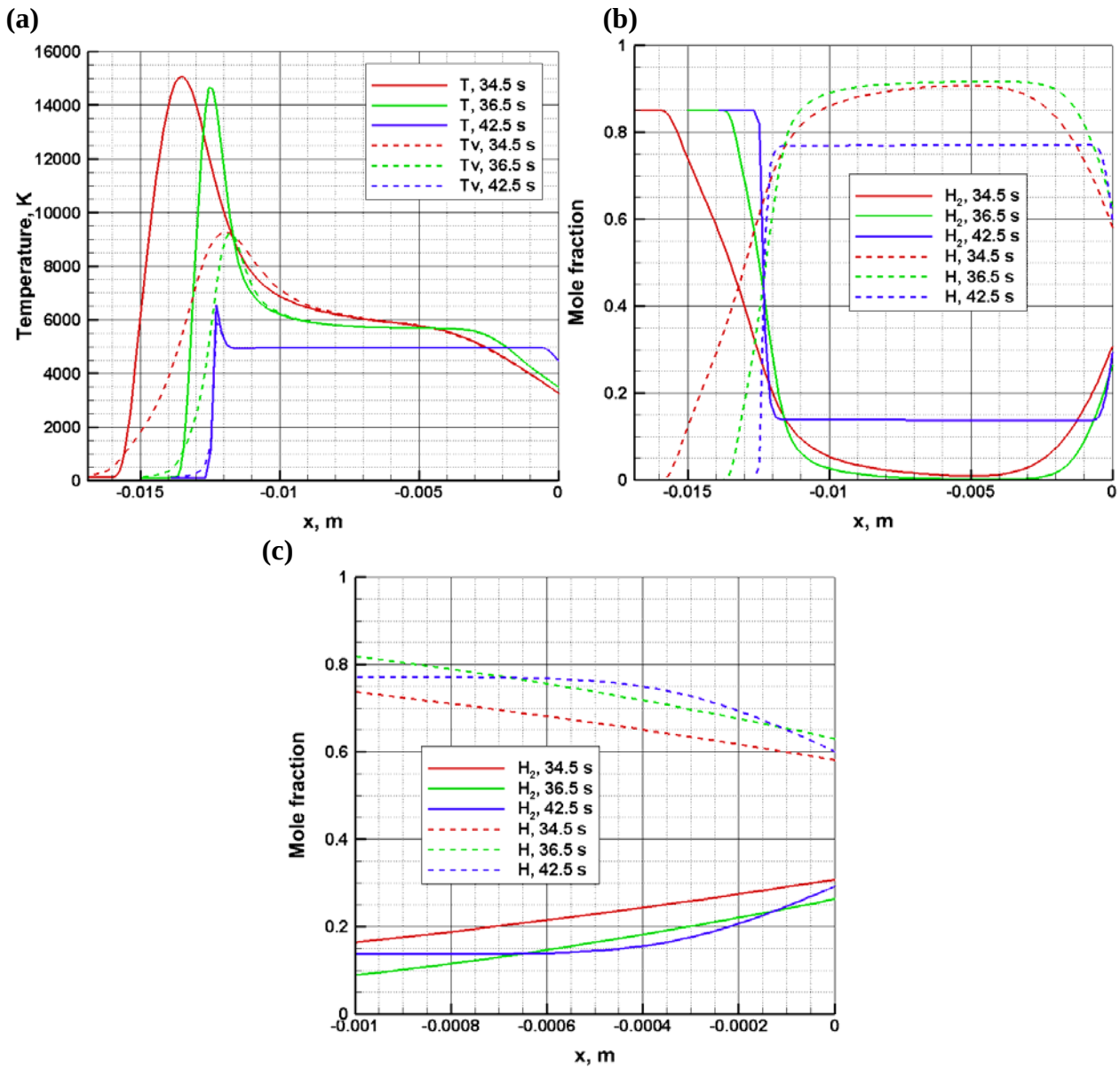

Figure 2. Stagnation line profiles for Uranus entries. (a) temperature (b) mole fractions (c) mole fractions near wall.

The first stage in the Monte Carlo process is to generate nominal *DPLR* CFD solutions from which the Monte Carlo CFD solutions are based. Stagnation line profiles for the three Uranus entry conditions are shown in Figure 4. The temperature and mole fraction profiles indicate that the 34.5 s trajectory point exhibits the largest degree of nonequilibrium in the shock layer and the largest nonequilibrium relaxation zone behind the bow shock. The t=36.5 s trajectory point shows peak values of translational and vibrational temperatures that are similar to those at the t=34.5 s point, but the shock standoff distance and nonequilibrium relaxation zone are smaller at t=36.5 s. Neither of these two cases has fully relaxed to equilibrium. At t=42.5 s, the freestream density is approximately two orders of magnitude greater than the density at t=34.5 and 36.5 s, and the t=42.5 s the shock layer is essentially in equilibrium. The electron mole fraction is negligible for all three Uranus cases, so the shock layer gas mixtures consist almost entirely of H_2, H, and He.

The Monte Carlo results for the Uranus simulations using an equilibrium catalytic wall are summarized in Table 5. The table lists the fractional contribution to the overall convective heating rate variability for the most influential input parameters. For the 36.5 s and 42.5 s entry conditions, the dominant contributor to convective heating rate variability are the $\Omega^{(1,1)}$ collision integrals, which determines species diffusivity and vibrational thermal conductivity. The $\Omega^{(1,1)}$ collision integrals account for 60-80% of the overall variability. The boundary layer composition is primarily H_2 and H, explaining the dependence on this particular collision integral. Species diffusivity will determine the so-called reactive thermal conductivity, so the result suggests that this dominates translational thermal conductivity. The H_2 dissociation reaction is also a significant contributor to convective heating rate variability, with H as the third body. At the t=34.5 s trajectory point, H_2 dissociation is the largest contributor to the uncertainty and accounts for about 38% of the convective heating rate variability. This is believed to matter insofar as the reaction rate determines the composition, and hence overall mixture thermal conductivity (including reactive conductivity), in the boundary layer.

Table 5. Contributions of selected key input parameters to overall convective heating rate variability for Uranus entries with equilibrium catalytic wall.

Input parameter	t = 34.5 s	t = 36.5 s	t = 42.5 s
$\Omega^{(1,1)}(H_2\text{-}H)$	0.347	0.604	0.802
$H + H_2 \leftrightarrow H + H + H$	0.419	0.077	0.005
$\Omega^{(1,1)}(H\text{-}He)$	0.103	0.223	0.134
$H_2 + H_2 \leftrightarrow H_2 + H + H$	0.012	0.002	< 0.002
$\Omega^{(1,1)}(H_2\text{-}He)$	0.006	0.013	0.017
$\Omega^{(2,2)}(H\text{-}H)$	0.036	0.036	0.006
Millikan-White 'a' (H_2-H)	0.029	< 0.002	< 0.002
$H_2 + H_2^+ \leftrightarrow H_2^+ + H + H$	< 0.002	0.003	0.002
Overall 2σ	± 2.1%	± 1.7%	± 1.2%

The Monte Carlo simulations can also be used to determine the spread in convective heating rates due to input parameter variability. Histograms of convective heating rates for the three Uranus cases

are shown in Figure 5. The plots show the number of Monte Carlo solution heating rates that were within a given range. The 2σ ranges of convective heating rates are fairly narrow for the Uranus simulations, ranging from ± 1.2% for the t=42.5 s condition to about ± 2.1% for the t=34.5 s condition.

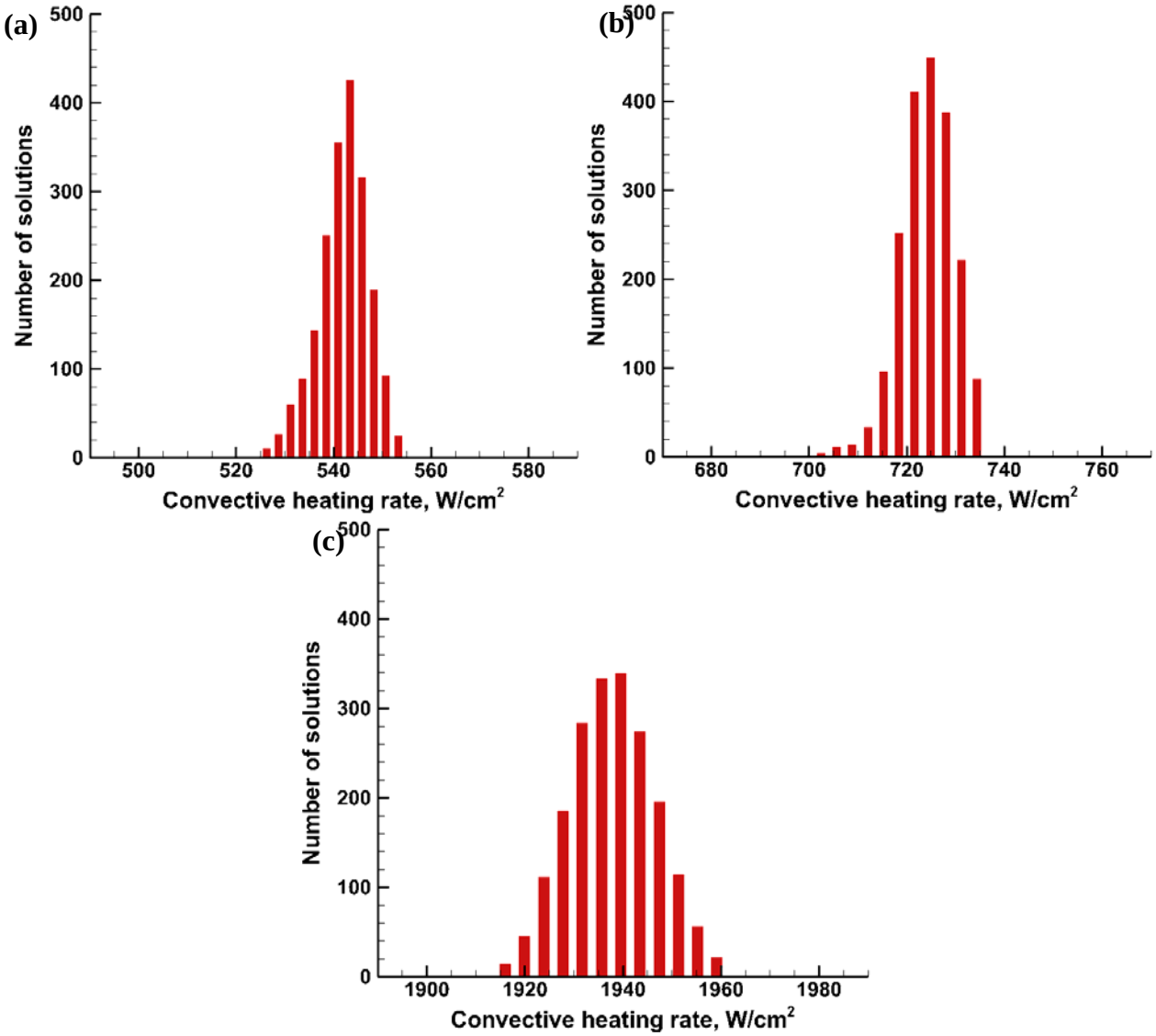

Figure 5. Convective heating rate histograms for Uranus entries. (a) t = 34.5 s (b) t = 36.5 s (c) t = 42.5 s.

The initial Uranus Monte Carlo simulations were generated under the assumption of an equilibrium catalytic wall, which would drive the wall species mole fractions to equilibrium values. Equilibrium mole fractions are a function of thermodynamic conditions (i.e. pressure and temperature) only and are largely independent of reaction rates. To investigate the effect of changing the wall catalysis model, a series of Monte Carlo simulations were performed at the t=34.5 s condition with different wall boundary conditions. The catalytic wall parameter, γ, was set to a non-catalytic wall (γ = 0) as well as a partially catalytic value, γ = 0.03. The values of γ used in the study along with the stagnation point values of convective heating rate, radiative heating rate, and radiative equilibrium wall temperature are shown in Table 6. As would be expected, convective heating rate and radiative

equilibrium wall temperature increase with increasing γ values. There was no effect on radiative heating. The equivalent equilibrium γ value at t=34.5 s was approximately 0.045. Nominal stagnation line temperature and atomic hydrogen mole fraction profiles near the wall are shown in Figure 6. The trends are as expected - wall temperature increases with increasing γ and atomic hydrogen mole fraction decreases.

Table 6. Stagnation point wall conditions for wall catalysis study, Uranus Monte Carlo simulations.

γ	q_w(conv) , W/cm^2	q_w(rad) W/cm^2	T_w K	C_H kg/m^2.s
0.0	176	4.6	2459	0.030
0.03	459	4.5	3125	0.040
equilibrium	542	4.6	3258	0.042

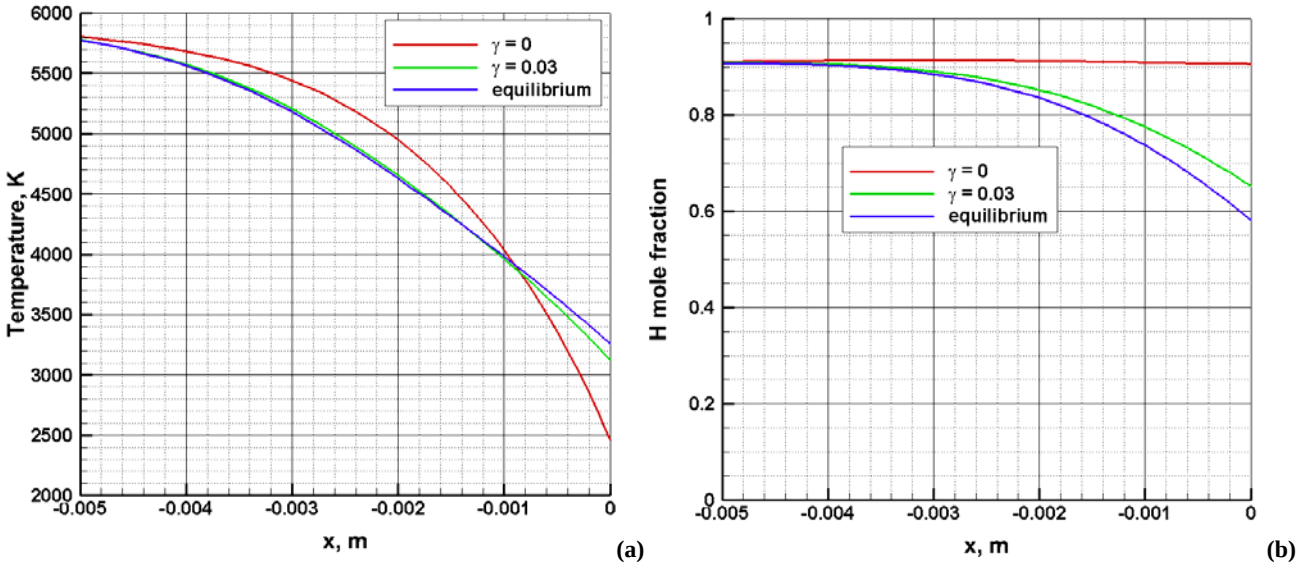

(a) (b)

Figure 6. Stagnation line profiles for Uranus t =34.5 s entry. (a) temperature, (b) atomic hydrogen mole fraction

The input parameters that contribute the most to convective heating rate variability for the t=34.5 s cases with varying catalytic wall conditions are shown in Table 7. As previously mentioned, the $\Omega^{(1,1)}$ collision integral and H recombination rates are the dominant input parameters by controlling reactive thermal conductivity in the boundary layer. For the partially catalytic case, the magnitude of catalytic heating is strongly dependent upon mole fractions at the wall, hence increasing the sensitivity to gaseous recombination rate and reducing the sensitivity to transport coefficients. For the non-catalytic wall, the concentration gradient is small and heat transfer is driven mainly by the translational thermal conductivity of H. Besides this dominant mechanism, many input parameters (including several not shown in Table 7) contribute in the 1-2% range.

Deviating from the equilibrium catalysis assumption increases the spread of the Monte Carlo stagnation point convective heating rate results. Histograms of convective heating rate for the γ = 0.03 and non-catalytic cases are shown in Figure 7. Both cases show a non-Gaussian profile shape, with extended tails at the high end of the range. The 2σ ranges of convective heating rates for the Uranus simulations ranged from approximately ± 18% for the non-catalytic condition to ± 2.1% for the equilibrium-catalytic solutions.

Table 7. Contributions of selected key input parameters to overall convective heating rate variability - Uranus *t* = 34.5 s conditions.

Input parameter	$\gamma = 0$	$\gamma = 0.03$	Equilibrium
$\Omega^{(1,1)}(H_2\text{-}H)$	0.01	0.022	0.347
$H + H_2 \leftrightarrow H + H + H$	0.312	0.884	0.419
$\Omega^{(1,1)}(H\text{-}He)$	< 0.002	< 0.002	0.103
$H_2 + H_2 \leftrightarrow H_2 + H + H$	0.043	0.004	0.012
$\Omega^{(1,1)}(H_2\text{-}He)$	< 0.002	< 0.002	0.006
$\Omega^{(2,2)}(H\text{-}H)$	0.565	0.039	0.036
Millikan-White '*a*' (H_2-H)	0.006	0.010	< 0.002
$\Omega^{(1,1)}(H\text{-}He)$	0.006	< 0.002	< 0.002
$H + He \leftrightarrow H^+ + e^- + He$	0.010	< 0.002	< 0.002
Overall 2σ	± 18%	± 6.8%	± 2.1%

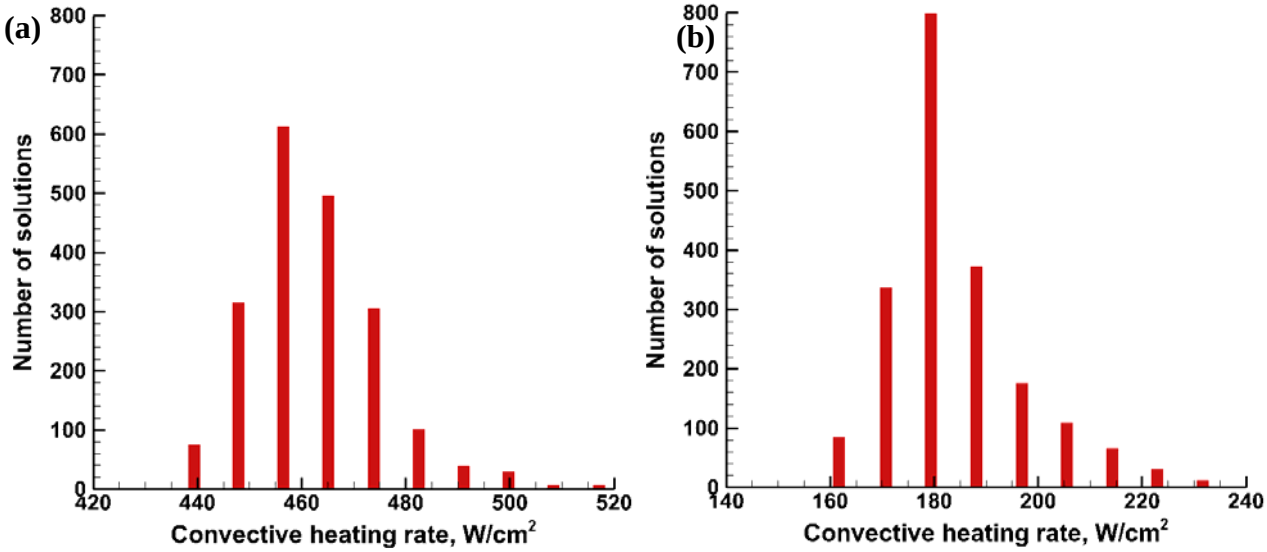

Figure 7. Convective heating rate histograms for Uranus t = 34.5 s entries. (a) γ = 0.03 (b) non-catalytic wall

The change in convective heating rate with recombination coefficient arises from the energy imparted to the surface when two hydrogen atoms recombine on its surface. The wall surface, being colder than the shocked gas, tends to cause recombination of free hydrogen atoms which are blown in from the shock layer. The sensitivity to reaction rate arises as the concentration of hydrogen atoms at the wall depends on how much recombination occurs within the boundary layer gas phase. It must be noted that the recombination model uses irreversible kinetics, so that if the system is near to equilibrium, the result will overpredict the amount of recombination on the wall. It also should be noted that the actual wall temperature may be lower than the predicted radiative equilibrium due to the heat capacity of the aeroshell and probe under finite entry time. The trade-off between temperature and wall recombination coefficients is shown schematically in Figure 8. The effective chemical and radiative equilibrium curves are interpolated from the CFD cases and are specific to the *t*=34.5s point on this trajectory. The kinetic curve is based on an activated process with activation energy given by the hydrogen recombination rate on pyrolytic graphite (8.4 kJ/mol).[43] The appropriate value of γ to use is most likely given by either the kinetic or chemical equilibrium line, whichever is less.

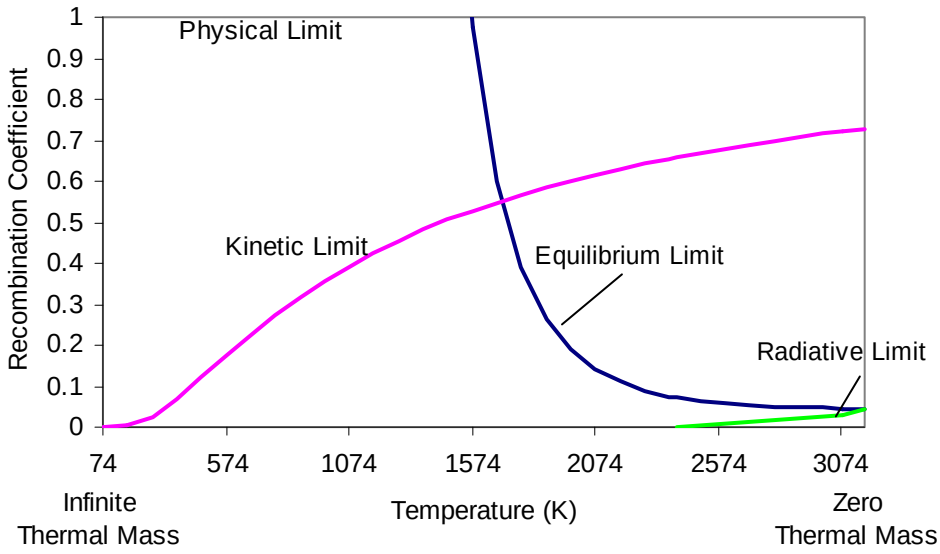

Figure 8. Schematic of valid values for recombination coefficient versus temperature

To further evaluate the catalysis dependency, the film coefficient was computed for each case simulated. The film coefficient is typically used as the input to a material response model which should derive a more physically accurate heating rate than is obtained directly from CFD. The film coefficient (C_H) is defined as:

$$C_H = \frac{q}{H_e - h_w} \tag{3}$$

where q is the heat flux, H_e is the enthalpy at the boundary layer edge and h_w is the enthalpy at the wall. On the stagnation line, $H_e = V^2/2$. Film coefficients are given in Table 6. It can be seen that the variation in film coefficient is much less than the variability in heat flux. The variation with γ is as large as 35%, which is greater than the 2σ due to all other parameters. Given the amount of variation in heating with recombination rate, the recommended best practice for further study would be to

employ a coupled material response and CFD model. In the absence of such a capability, equilibrium wall is recommended since this would bound γ at reasonably expected surface temperatures.

Results - Saturn Entries

Three trajectory points were analyzed for the 1.0 m diameter, 45-degree sphere cone geometry entering the atmosphere of Saturn. The first two cases were for the 216 kg, 45-degree sphere cone vehicle entering Saturn on the decadal trajectory. A third set of simulations were performed for the heavier, 250 kg, capsule with higher entry velocity of 28.2 km/s (atmosphere relative). The freestream conditions, stagnation point convective and radiative heating rates, and radiative equilibrium wall temperatures are shown in Table 8. Freestream mass fractions were assumed to be 0.803 and 0.197 for H_2 and He respectively (0.89 and 0.11 by mole fraction). The t = 272 s condition represents the peak convective heating point on the 216 kg decadal trajectory, per *TRAJ*. The convective heating from CFD is as much as 40% less than the *TRAJ* prediction, while the *NEQAIR* radiative heating is about half the amount predicted by *TRAJ*. Because radiative heating is significant (up to 15% of total heating) for the t = 91.5 s trajectory point, Monte Carlo simulations were performed for both convective and radiative heating rates at this conditions, while convective heating alone was analyzed for the t = 206 s and 272 s trajectory points. All of the Saturn CFD solutions were computed with an equilibrium catalytic wall assumption.

Table 8. Freestream and wall conditions, Saturn Monte Carlo simulations.

Entry mass kg	t s	ρ_∞ kg/m^3	T_∞ K	V_∞ km/s	q_w(conv) W/cm^2	q_w(rad) W/cm^2	T_w, K
216	206	1.80e-5	141.0	26.316	690	34	3459
216	272	6.30e-5	141.2	23.466	790	4.4	3578
250	91.5	5.77e-5	141.2	27.706	1208	133	3978

Stagnation line profiles for the nominal Saturn *DPLR* CFD solutions are shown in Figure 9. Temperature profiles in Figure 9(a) indicate that the largest nonequilibrium relaxation zone is with the 216 kg, t = 206 s condition. The shock layer temperatures are the highest for the 250 kg, t = 91.5 s case, as would be expected. In all three cases, the degree of H_2 dissociation exceeds 99.9%. Although all three cases display a substantial zone of steady temperature and H mole fraction, the ionization rates are sufficiently slow that the electron fraction is increasing throughout the shock layer. As a result, the two lowest density cases have a steady temperature that exceeds equilibrium by 2000-3000K. This steady temperature does not begin to relax toward its equilibrium value until the electron fraction reaches on the order of 1%, which only occurs in the 250 kg, t= 91.5 s case. For the 216 kg, t= 272s case, the equilibrium electron fraction is sufficiently small that the temperature and neutral mole fractions are approximately in equilibrium throughout the shock layer.

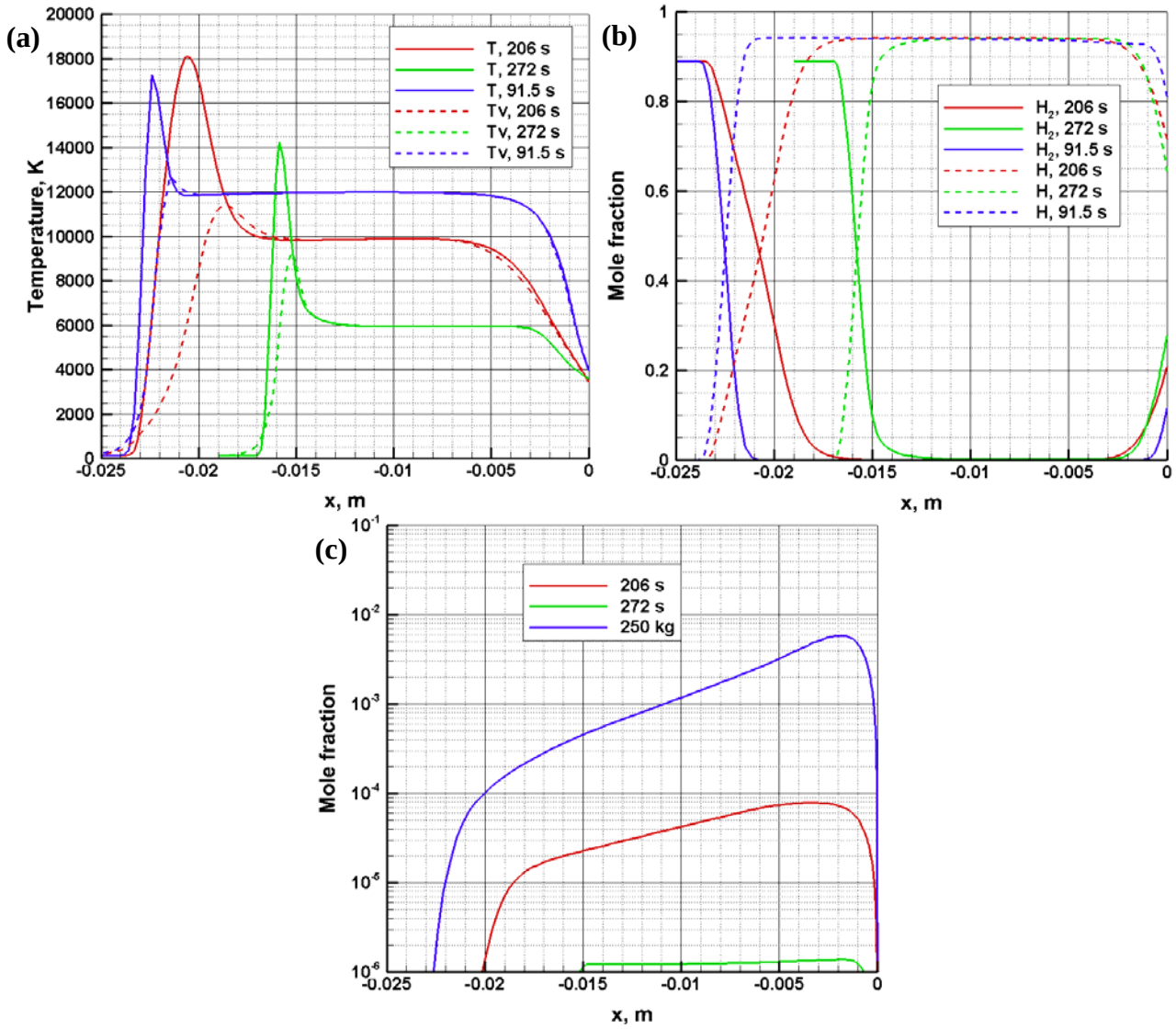

Figure 9. Stagnation line profiles for Saturn entries: (a) temperature, (b) H_2 and H mole fractions, and (c) electron mole fraction.

The *DPLR* input parameters that contributed the most to convective heating rate variability for the Saturn entries are shown in Table 9. All three cases were run assuming an equilibrium catalytic wall. For the 216 kg vehicle at t= 206 and 272 s, the convective heating rate variability is largely influenced by the $\Omega^{(1,1)}$ and $\Omega^{(2,2)}$ collision integrals, together accounting for 80-90% of the overall variability. The species mole fractions are driven towards equilibrium values at the wall, so the effect of chemical reaction rates on convective heating is minimal. For the heavier 250 kg vehicle at t= 91.5 s, the ionization reactions throughout the shock layer drive the temperature at the boundary layer edge, and this dominates the variability in convective heating.

Table 9. Contributions of selected key input parameters to convective heating rate variability for Saturn entries.

Input parameter	t = 206 s	t = 272 s	t = 91.5 s
$\Omega^{(2,2)}$(H-H)	0.325	0.029	0.146
$\Omega^{(1,1)}$(H-He)	0.155	0.109	0.066
$\Omega^{(1,1)}$(H_2-H)	**0.429**	**0.730**	0.026
$H + H_2 \leftrightarrow H + H + H$	0.033	0.080	0.007
$H + H \leftrightarrow H + e^- + H^+$	< 0.002	< 0.002	**0.226**
$\Omega^{(1,1)}$ (H_2-He)	0.008	0.010	< 0.002
Millikan-White '*a*' (H-He)	0.010	< 0.002	< 0.002
$H + He \leftrightarrow H^+ + e^- + He$	< 0.002	< 0.002	0.005
$\Omega^{(1,1)}$ (H-H^+)	0.003	< 0.002	0.018
$H + e^- \leftrightarrow e^- + e^- + H^+$	< 0.002	< 0.002	**0.452**
Overall 2σ	± 1.5%	± 1.6%	± 3.7%

Convective heating rate histograms for the three Saturn entry conditions are shown in Figure 10. The 2σ range of convective heating rate for the 216 kg, t = 206 s case was ± 1.5%, and it was ± 1.5% for the 216 kg, t= 272 s conditions. For the heavier entry mass vehicle at t= 91.5 s, the 2σ range on convective heating rate was larger, approximately ± 3.7%.

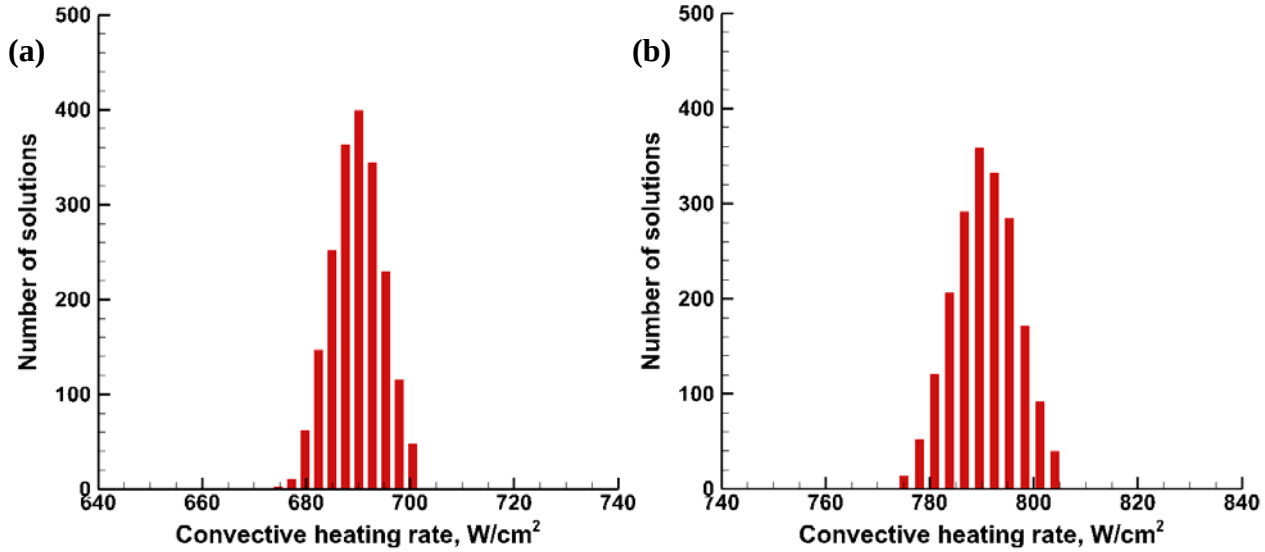

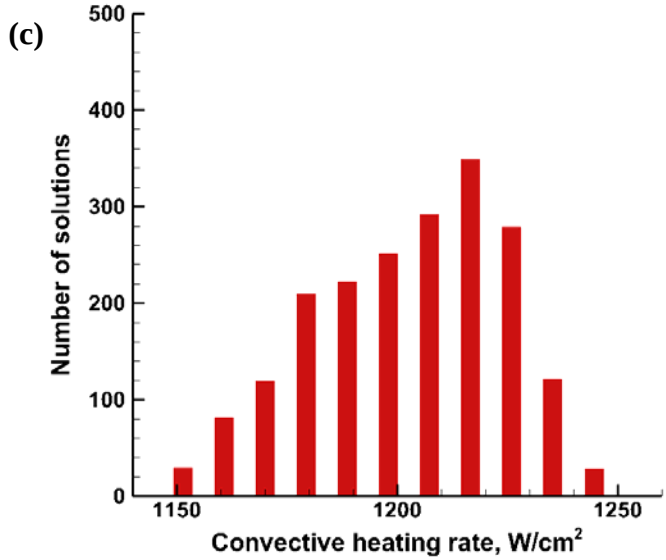

Figure 10. Convective heating rate histograms for Saturn entries. (a) *t* = 206 s (b) *t* = 272 s (c) *t* = 91.5 s.

Because the Saturn *t*= 206 s nominal solution showed significant levels of stagnation point radiative heating, a Monte Carlo analysis on radiative heating was performed for this condition as well. For these simulations, the existing Monte Carlo *DPLR* CFD solutions were used to provide temperatures and species number densities along the stagnation point line-of-sight to the *NEQAIR* line-by-line radiation code. The *NEQAIR* spectral database inputs were not varied during the analysis, so the results represent the *DPLR* CFD inputs that have the greatest impact on stagnation point radiative heating rates.

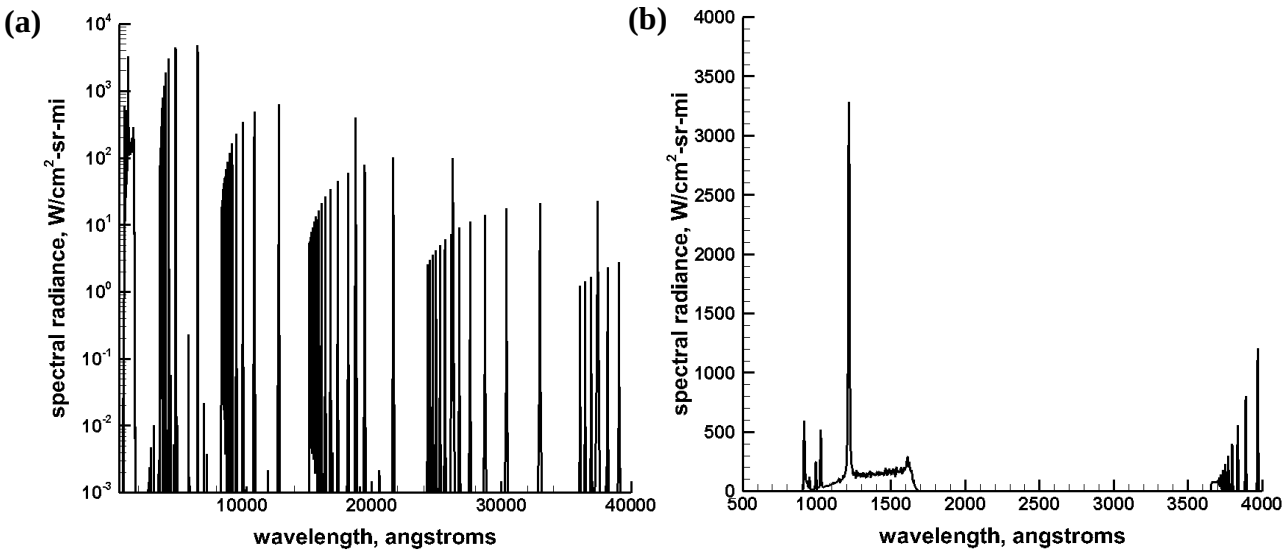

Figure 11. Radiative spectrum for Saturn 250 kg, t = 91.5 s entry. (a) results for spectral range 800 - 40000 angstroms (b) close-up between 800 - 4000 angstroms.

The spectral radiance as a function of wavelength for the 250 kg, *t*= 91.5 s case is shown in Figure 11. The spectral range between 600 - 40000 angstroms is shown in Figure 11(a), and a close-up

between 600 - 4000 angstroms is presented in Figure 11(b). The primary radiators are the H_2 (B-X) band system, that exists in the vacuum ultraviolet (VUV) region between 900 - 1700 angstroms and atomic hydrogen lines that exist throughout the spectral range. Atomic hydrogen lines account for approximately 75% of the overall spectral radiance, and the H_2 (B-X) band system accounts for 24% of the overall spectral radiance.

Table 10. Contributions of selected key input parameters to radiative heating rate variability for Saturn entries.

Input parameter	t = 91.5 s
$H + H_2 \leftrightarrow H + H + H$	0.861
Millikan-White '*a*' (H_2-H)	0.029
$\Omega^{(1,1)}$(H-H)	0.011
$\Omega^{(2,2)}$(H-H)	0.010
Millikan-White '*b*' (H_2^+-H)	0.008
Millikan-White '*a*' (H_2- H_2)	0.006
$\Omega^{(2,2)}$(H_2-e^-)	0.005
$H + H \leftrightarrow H + e^- + H^+$	0.004

The *DPLR* CFD input parameters that contribute the greatest to radiative heating rate variability are shown in Table 10. Unlike convective heating, which is determined by the shape and characteristics of the boundary layer, radiative heating is primarily influenced by the radiative environment that occurs just downstream of the bow shock wave. Chemical reaction rates, particularly for the H_2 dissociation reaction, have the largest impact on radiative heating rate variability. Millikan-White V-T relaxation time constants have a minor influence, accounting for about 3-5% of the radiative heating rate variability. Collision integrals have a much smaller influence on radiative heating than was seen with convective heating.

Radiative heating rate histograms for the t = 91.5 s Saturn entry condition are shown in Figure 12. The radiative heating rate histograms show a distinct non-Gaussian character with a long "tail" evident for radiative heating rates greater than the mean value. Radiative heating rates at the surface are very sensitive to what happens just downstream of the shock. Changes in chemical reaction rates alter the relationship between temperature and species number density (the primary inputs to radiative heating) at the shock, which can significantly change the radiative heating rate experienced at the wall. The variability range for radiative heating rate is significantly larger than was seen with convective heating. The 2σ range on radiative heating rate for the t = 91.5 s case was approximately ± 63 - 280%. It is worth noting that the tail of these distributions are comparable to convective heating rates - so that neglecting radiation on the basis of nominal results could result in a substantial error in the overall heating magnitude.

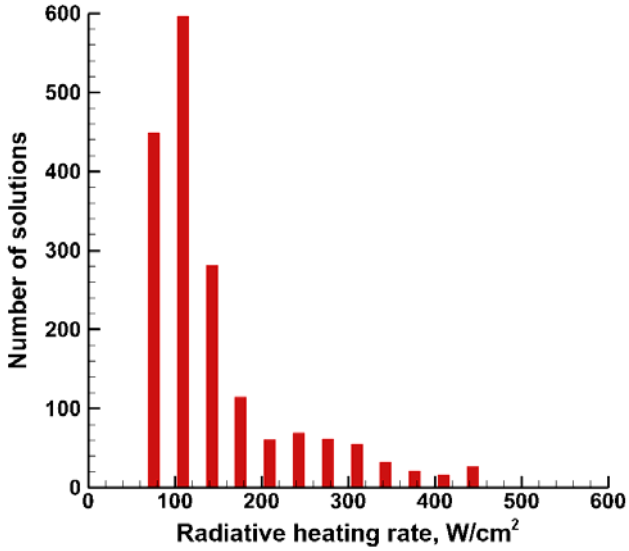

Figure 12. Radiative heating rate histograms for Saturn entry, t = 91.5 s.

Diffusion Model

In the work reported above, the self-consistent effective binary diffusion (SCEBD) model was employed. This model is an efficient and cost-effective replacement for a true multicomponent mass diffusion model, especially in situations where there are disparate masses in the gas mixture. However, many groups instead opt to employ a constant Schmidt (*Sc*) or Lewis (*Le*) number flow to simplify the calculation requirements. Many of the cases examined here were also repeated using a constant Schmidt number. The Schmidt number is sensitive to the reduced mass of the mixture. For these cases, it was found that a *Sc* = 0.5 best reproduced the nominal heating profiles. However, studies performed with constant Schmidt number showed significantly different sensitivities in the Monte Carlo analysis. This is because the constant Sc number removes any sensitivity to $\Omega^{(1,1)}$, and instead uses only $\Omega^{(2,2)}$ to determine all transport properties. Secondly, under a constant Schmidt number, the sensitivity of convective heating to H recombination rates was completely eliminated. This is because a constant Schmidt number will remove the sensitivity of the thermal conductivity to mixture composition, which is a function of reaction rates. Finally, the sensitivity of film coefficient to wall catalysis model was reduced to as little as 10% under constant Sc (as compared to 35% for SCEBD). On the basis of these observations, it is recommended that SCEBD be adopted as best practice for outer planets mission sizing studies.

V. Conclusions

An analysis of heating sensitivities for a future probe mission to Saturn or Uranus has been investigated. The results have keyed off of concept studies performed as part of the 2013-2022 Decadal Survey. Trajectories have been rebuilt using the *TRAJ* software for the entry conditions specified in the Decadal reports. The *TRAJ* trajectories have been analyzed for peak heating and regions of significant non-equilibrium heating which may be sensitive to shock-layer kinetics.

As part of this work, many of the input parameters to H_2-He CFD were more closely examined. Neutral collision integrals, which are found to be the major uncertainty driver, are determined to be known to high accuracy. However, many of the neutral-ion and neutral-electron collision integrals in *DPLR* were found to be dated and were revised in the *DPLR* CFD code, although these updates had small impact to the resulting predictions. The default translation-vibration relaxation time was found to be off by orders of magnitude. The new parameterization produced for pt_v had significant impact on temperature and number density profiles which will impact radiative heating, particularly for Saturn entry problems.

A Monte Carlo analysis was performed in order to determine which CFD input parameters had the greatest effect on convective and radiative heating rates for capsules entering the atmospheres of Uranus and Saturn. For the Uranus cases, the primary driver of convective heating rate variability with an equilibrium catalytic wall were the $\Omega^{(1,1)}$ collision integrals and the H + H recombination reaction, which together determine the reactive thermal conductivity within the boundary layer. If the catalytic recombination parameter, γ, is set to a value away from equilibrium, the convective heating rate becomes more influenced by the H+H recombination rate, which will determine the flux of H atoms contributing to catalytic wall heating. However, as γ is driven to zero, there will be no catalytic wall heating and the heat transfer is driven primarily by the translational thermal conductivity, which is determined by $\Omega^{(2,2)}$. For Saturn entry, the primary uncertainty driver changed depending on the entry condition. For the highest velocity condition examined (27.7 km/s), the temperature at the boundary layer edge was determined by the ionization fraction, hence leading to a strong sensitivity to H atom ionization rate. At slightly lower velocities (26.5 km/s) the ionization fraction did not become large enough to influence temperature and there was little recombination in the boundary layer, leading to a sensitivity on $\Omega^{(2,2)}$, similar to the non-catalytic wall Uranus case. At the lowest velocity of 26.3 km/s, the sensitivity was primarily to $\Omega^{(1,1)}$, as in the Uranus equilibrium wall case. However, the higher wall and boundary layer temperatures prevented the recombination rate from having significant impact. A cold wall simulation would be expected to show much higher sensitivity to boundary layer recombination.

This study has generated some recommended best-practices for future Outer Planets sizing missions. First, the self-consistent effective binary diffusion model is required in order to capture the variability in thermal conductivity within a reacting boundary layer. Second, since the film coefficient shows noticeable dependence on the wall catalysis model, a coupled CFD/Material response model is advisable. In the absence of such capability, however, a chemical equilibrium wall appears consistent with temperature predictions and expected H surface recombination kinetics, in addition to giving a more conservative estimate of heat flux and film coefficient.

While, in general, the uncertainty in the convective heating was no more than a few percent, the uncertainty in radiative heating was substantial. Radiative heating becomes a significant portion of the total heating when the shock layer temperature exceeds ~10,000K, which would be expected for a Saturn entry probe. Because radiative heating at the wall is strongly influenced by the temperature and species number density profiles just behind the bow shock, the strongest contributors to radiative heating rate variability were found to be the H_2 dissociation reaction rates. Collision integrals had only a minor impact on radiative heating rates. Here, the 2σ ranges of radiative heating rate variability were greater than 100%.

VI. Acknowledgements

The authors would like to thank Drs. Helen Hwang, Suman Muppiddi and Aaron Brandis for useful discussions. Dr. Michael Barnhardt is acknowledged for assistance with updating the DPLR databases and running test case comparisons. The authors are supported by NASA contract NNA10DE12C to ERC Corporation.

VII. References

1. Leibowitz, L. P., and Kuo, T. J., "Ionizational Nonequilibrium Heating During Outer Planetary Entries," *AIAA Journal*, Vol. 14, 1976, pp. 1324-1329.
2. Palmer, G., "Uncertainty Analysis of CEV LEO and Lunar Return Entries," AIAA Paper 2007-4253, June 2007.
3. Johnston, C.O. and Kleb, B., "Uncertainty Analysis of Air Radiation for Lunar-Return Shock Layers," *Journal of Spacecraft and Rockets*, Vol. 49, No. 3, 2012, pp. 435-450.
4. Palmer, G. E., Olejniczak, J., and Wright, M. J., "Uncertainty Analysis of Aeroheating Prediction for Titan Entries," AIAA Paper 2006-0388, January 2006.
5. Bose, D., Wright, M. J., and Gökçen, T., "Uncertainty and Sensitivity Analysis of Thermochemical Modeling for Titan Atmospheric Entry," AIAA Paper 2004-2455, July 2004.
6. Bose, D., Wright, M. J., and Palmer, G. E., "Uncertainty Analysis of Laminar Aeroheating Predictions for Mars Entries," *Journal of Thermophysics and Heat Transfer*, Vol. 20, No. 4, 2006, pp. 652-662.
7. Gnoffo, P. A., Weilmuenster, K. J., Hamilton, H. H., Olynick, D. R., and Venkatapathy, E., "Computational Aerothermodynamic Design Issues for Hypersonic Vehicles," *Journal of Spacecraft and Rockets*, Vol. 36, No. 1, 1999, pp. 21-43.
8. National Research Council, *Vision and Voyages for Planetary Science in the Decade 2013-2022*, National Academies Press, 2012.
9. Wright, M. W., White, T., and Mangini, N., "Data Parallel Line Relaxation (DPLR) Code User Manual Acadia – Version 4.01.1," NASA/TM-2009-215388, October 2009.
10. Spilker, T. R., "Saturn Atmospheric Entry Probe Trade Study," *Vision and Voyages for Planetary Science in the Decade 2013-2022*, National Academies Press, 2010.
11. Spilker, T. R., "Saturn Atmospheric Entry Probe Mission Study," *Vision and Voyages for Planetary Science in the Decade 2013-2022*, National Academies Press, 2010.
12. Hubbard, W. B., "Ice Giants Decadal Study," *Vision and Voyages for Planetary Science in the Decade 2013-2022*, National Academies Press, 2010.
13. Allen, G. A., Wright, M. J., and Gage, P., "The Trajectory Program (Traj): Reference Manual and User Guide," NASA/TM-2004-212847, 2005.
14. Palmer, G. E., and Wright, M. J., "A Comparison of Methods to Compute High Temperature Gas Thermal Conductivity," AIAA Paper 2003-3913, June 2003.

15. Wright, M. J., Hwang, H. H., and Schwenke, D. W., "Recommended Collision Integrals for Transport Property Computations Part 2: Mars and Venus Entries," *AIAA Journal*, Vol. 45, No. 1, 2007, pp. 281-288.
16. Wright, M. J., Bose, D., Palmer, G. E., and Levin, E., "Recommended Collision Integrals for Transport Property Computations Part 1: Air Species," *AIAA Journal*, Vol. 43, No. 12, 2005, pp. 2558-2564.
17. Wright, M. J., and Levin, E., "Recommended Collision Integrals for Transport Property Computations, Part 3: Giant Planet Entries," *unpublished*.
18. Bruno, D., Catalfamo, C., Capitelli, M., Colonna, G., De Pascale, O., Diomede, P., Gorse, C., Laricchiuta, A., Longo, S., Giordano, D., and Pirani, F., "Transport properties of high-temperature Jupiter atmosphere components," *Physics of Plasmas,* Vol. 17, 2010, p. 112315.
19. Gupta, R. N., Yos, J. M., Thompson, R. A., and Lee, K. P., "A Review of Reaction Rates and Thermodynamic and Transport Properties for an 11-Species Air Model for Chemical and Thermal Nonequilibrium Calculations to 30000 K," NASA RP-1232, 1990.
20. Stallcop, J. R., Levin, E., and Partridge, H., "Transport Properties of Hydrogen," *Journal of Thermophysics and Heat Transfer,* Vol. 12, No. 4, 1998, pp. 514-519.
21. Stallcop, J. R., Partridge, H., and Levin, E., "H—H2 collision integrals and transport coefficients," *Chemical Physics Letters,* Vol. 254, No. 1, 1996, pp. 25-31.
22. Yos, J. M., "Transport Properties of Nitrogen, Hydrogen, Oxygen, and Air to 30,000 K," Tech. Memo. RAD-TM-63-7 (Contract AF33(616)-7578), AVCO Corp., March 1963.
23. Krstic, P. S., and Schultz, D. R., "Elastic processes involving vibrationally excited molecules in cold hydrogen plasmas," *Journal of Physics B: Atomic, Molecular and Optical Physics,* Vol. 36, No. 2, 2003, p. 385.
24. Krstic, P. S., and Schultz, D. R., "Elastic scattering and charge transfer in slow collisions: isotopes of H and H+ colliding with isotopes of H and with He," *Journal of Physics B: Atomic, Molecular and Optical Physics,* Vol. 32, No. 14, 1999, p. 3485.
25. Laricchiuta, A., Colonna, G., Bruno, D., Celiberto, R., Gorse, C., Pirani, F., and Capitelli, M., "Classical transport collision integrals for a Lennard-Jones like phenomenological model potential," *Chemical Physics Letters,* Vol. 445, No. 4, 2007, pp. 133-139.
26. Bray, I., Konovalov, D. A., and McCarthy, I. E., "Coupled-channel optical calculation of electron-hydrogen scattering: Elastic scattering from 0.5 to 30 eV," *Physical Review A,* Vol. 43, No. 11, 1991, p. 5878.
27. Gupta, G. P., and Mathur, K. C., "Differential cross sections for the elastic scattering of electrons by hydrogen atoms at intermediate energies," *Journal of Physics B: Atomic and Molecular Physics,* Vol. 13, 1980, p. 1719.
28. Brunger, M. J., and Buckman, S. J., "Electron–molecule scattering cross-sections. I. Experimental techniques and data for diatomic molecules," *Physics reports,* Vol. 357, No. 3, 2002, pp. 215-458.
29. Shyn, T. W., and Sharp, W. E., "Angular distributions of electrons elastically scattered from H_2," *Physical Review A,* Vol. 24, No. 4, 1981, p. 1734.
30. Biagi, S., http://rjd.web.cern.ch/rjd/cgi-bin/cross, 2008.
31. Aubreton, J., Elchinger, M. F., Fauchais, P., Rat, V., and André, P., "Thermodynamic and transport properties of a ternary Ar–H2–He mixture out of equilibrium up to 30 000 K at atmospheric pressure," *Journal of Physics D: Applied Physics,* Vol. 37, No. 16, 2004, p. 2232.

32. Aubreton, J., Elchinger, M. F., Rat, V., and Fauchais, P., "Two-temperature transport coefficients in argon–helium thermal plasmas," *Journal of Physics D: Applied Physics,* Vol. 37, No. 1, 2003, p. 34.
33. Rundel, R. D., Nitz, D. E., Smith, K. A., Geis, M. W., and Stebbings, R. F., "Resonant charge transfer in He^+-He collisions studied with the merging-beams technique," *Physical Review A,* Vol. 19, No. 1, 1979, p. 33.
34. Yevseyev, A. V., Radtsig, A. A., and Smirnov, B. M., "The asymptotic theory of resonance charge exchange between diatomics," *Journal of Physics B: Atomic and Molecular Physics,* Vol. 15, No. 23, 1982, p. 4437.
35. Millikan, R. C., and White, D. R., "Systematics of Vibrational Relaxation," *Journal of Chemical Physics,* Vol. 39, 1963, pp. 3209-3213.
36. Kim, J. G., Kwon, O. J., and Park, C., "Master Equation Study and Nonequilibrium Chemical Reactions for H + H_2 and He + H_2," *Journal of Thermophysics and Heat Transfer,* Vol. 23, No. 3, 2009, pp. 443-453.
37. Park, C., "Nonequilibrium Ionization and Radiation in Hydrogen–Helium Mixtures," *Journal of Thermophysics and Heat Transfer,* Vol. 26, No. 2, 2012, pp. 231-243.
38. Dove, J. E., and Teitelbaum, H., "The vibrational relaxation of H_2. I. Experimental measurements of the rate of relaxation by H_2, He, Ne, Ar, and Kr," *Chemical Physics,* Vol. 6, No. 3, 1974, pp. 431-444.
39. Wright, M. J., Bose, D., and Chen, Y. K., "Probabilistic Modeling of Aerothermal and Thermal Protection Material Response Uncertainties," *AIAA Journal,* Vol. 45, No. 2, 2007, pp. 399-410.
40. Whiting, E., Park, C., Liu, Y., Arnold, J., and Paterson, J., "NEQAIR96, Nonequilibrium and Equilibrium Radiative Transport and Spectra Program: User's Manual," NASA RP-1389, 1996.
41. Brandis, A. M., Cruden, B. A., Prabhu, D., Johnston, C. O., and Bose, D., "Uncertainty Analysis of NEQAIR and HARA Predictions of Air Radiation Measurements Obtained in the EAST Facility," AIAA Paper 2011-3478, June 2011.
42. Cruden, B. A., Prabhu, D., and Martinez, R., "Absolute Radiation Measurement in Venus and Mars Entry Conditions," *Journal of Spacecraft and Rockets,* Vol. 49, No. 6, 2012, pp. 1069-1079.
43. King, A. B., and Wise, H., "Reaction kinetics of hydrogen atoms with carbon films," *The Journal of Physical Chemistry,* Vol. 67, No. 6, 1963, pp. 1163-1170.